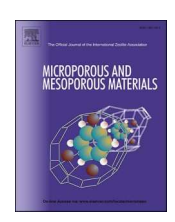
ELSEVIER

Contents lists available at ScienceDirect

Microporous and Mesoporous Materials

journal homepage: www.elsevier.com/locate/micromeso





Determination of film thicknesses of metal oxides prepared by atomic layer deposition on SBA-15

Ching-Yu Wang ^{a,1}, Benjamin T. Ferko ^{b,1}, Kai Shen ^a, Karen I. Winey ^{a,b}, John M. Vohs ^{a,*}, Raymond J. Gorte ^{a,b}

- ^a Department of Chemical and Biomolecular Engineering, University of Pennsylvania, Philadelphia, PA, 19104, USA
- ^b Department of Materials Science and Engineering, University of Pennsylvania, Philadelphia, PA, 19104, USA

ARTICLE INFO

Keywords: Atomic layer deposition Mesoporous silica Small-angle X-ray scattering N_2 isotherm BJH method Pore size distribution Thin film Density

ABSTRACT

 $\rm ZrO_2$ and $\rm CeO_2$ films were grown in SBA-15 by Atomic Layer Deposition (ALD) to loadings of 0.92 g oxide/g SBA-15. Scanning Transmission Electron Microscopy (STEM) with Energy Dispersive Spectra (EDS) showed that the oxides grew uniformly inside the mesopores. Film thicknesses were then analyzed as a function of the number of ALD cycles using three methods: 1) mass changes assuming bulk densities for the films; 2) changes in pore size from Barret-Joyner-Halenda (BJH) analysis with $\rm N_2$ adsorption isotherms; and 3) small-angle X-ray scattering (SAXS). Film thicknesses assuming bulk densities were between 6 and 8 times smaller than those obtained from BJH analysis. SAXS analysis gave film thicknesses that were approximately twice that obtained from bulk densities. Possible explanations of the discrepancies between these methods are discussed.

1. Introduction

Mesoporous materials, like SBA-15 and MCM-41, have intriguing properties for catalytic applications because of their well-defined, uniform, pore structures [1–4]. The pore sizes are somewhat tunable and extend the range of available pore diameters beyond that which can be achieved in zeolites [5]. They are prepared by allowing silica to condense out of an aqueous solution in the presence of surfactant. Mesoporous oxides having compositions other than silica can be prepared by analogous methods [6–8], but the silica-based materials are by far the most common because of their relatively high stability and ease of synthesis.

Another way to vary the composition of mesoporous materials involves coating the pores of silica-based materials with a second oxide. Although coatings can be added by conventional infiltration [9], conformal coatings of variable thickness are most easily prepared by Atomic Layer Deposition (ALD) [10–14]. In ALD, a solid surface is exposed to a precursor molecule which then reacts with that surface to form an adsorbed monolayer. After removing excess precursor, the adsorbed molecules are oxidized to remove the ligands and form an oxide film. By repeating this process, films of variable thickness can be prepared. With mesoporous materials that have pores only moderately

larger than the film thickness, the added films can reduce the size of the pores, in addition to changing the composition of those pores.

Two different methods have been proposed for calculating the film thickness of ALD films and the resulting decrease in pore size of a modified mesoporous material [10,15]. The first method uses N2 isotherms and the Barret-Joyner-Halenda (BJH) method to determine the pore sizes of the material before and after film addition [15,16]. Because SBA-15 has pores that are very uniform in size, the film thickness can be determined quite accurately from the changes in the pore size distribution. Alternatively, because the mass of even thin films added to high-surface-area materials can be significant, the film thickness can be estimated from the mass of the film, assuming that the density of the film is the same as that of the bulk oxide [10]. For example, a 0.5-nm film of ZrO_2 on a 600-m²/g SBA-15 would have 1.70 g ZrO_2 /g of SBA-15 (63-wt % ZrO₂). This calculation is also interesting because it provides an upper limit as to how thick the films can be. SBA-15 with even a 0.5-nm film will have a significantly lower specific surface area, both due to the change in mass of the sample and the smaller pore size.

Unfortunately, it has been shown that these two methods for calculating film thickness and pore-size changes give dramatically different results. In a study of $\rm ZrO_2$ films in SBA-15, BET results for a sample with 0.90 g $\rm ZrO_2/g$ SBA-15 (48-wt% $\rm ZrO_2$) showed a decrease in pore size

E-mail address: vohs@seas.upenn.edu (J.M. Vohs).

^{*} Corresponding author.

 $^{^{1}\,}$ The authors contribute equally.

from 9.0 nm to 6.6 nm, implying a nominal $\rm ZrO_2$ film thickness of 1.2 nm [10]. The film thickness calculated from the mass change on this material was 0.25 nm, a factor of 4.8 smaller. It is possible that the density of the oxide film is lower than that of the bulk, but the discrepancy here seems to be too large. There could also be a contraction of the SBA-15 structure; however, this would result in a decrease in the distance between pore centers, which was not observed in X-ray diffraction (XRD) [10].

In the present study we set out to further investigate the accuracy of BJH analysis of N₂ adsorption isotherms and gravimetric measurements to determine the thicknesses of conformal films of ZrO2 and CeO2 grown on mesoporous SBA-15 by ALD. To provide insight into the accuracy of each technique we also used analysis of small-angle X-ray scattering (SAXS) diffraction data to estimate film thicknesses. The uniform linear pore structure of SBA-15 facilitates the use of SAXS for this purpose and allows one to obtain an accurate measure of pore diameter and film thickness. The results of this study showed that film thicknesses estimated from BJH analysis of N2 adsorption isotherms were substantially larger than those determined from SAXS which is consistent with previous studies that have concluded that BJH analysis underestimates pore sizes for mesoporous materials with pores less than 10 nm in diameter [17,18]. Pore sizes determined from the weight change and assuming the oxide film had the same density as the corresponding bulk material were found to be in better accord with those determined by SAXS but still systematically underestimated the film thickness. Possible explanations for the discrepancies between the values derived from these methods are also discussed.

2. Materials and methods

SBA-15 was synthesized following a procedure described in the literature [4,5,19–21]. Initially, 4.0 g of Pluronic P-123 (Sigma-Aldrich) was dissolved in a solution containing 120 g of 2 M HCl and 30 g of deionized water at 298 K. 8.5 g of tetraethoxysilane (TEOS, Sigma-Aldrich, 99 %) was then added dropwise at 308 K with stirring for 20 h at the same temperature. The solution was then maintained at 373 K for 24 h to facilitate TEOS hydrolysis. The resulting solution was filtered, washed with deionized water, and dried at 353 K for 8 h. Finally, to remove the P-123, the sample temperature was ramped at 1 K/min in flowing air to 773 K and held at that value for 6 h. The resulting SBA-15 had well-defined, one-dimensional, 9.45-nm pores and a surface area of 785 m²/g, as determined by N_2 adsorption isotherms and transmission electron microscopy (TEM). The details of the characterization have been reported in previous study [10].

ALD of ZrO $_2$ and CeO $_2$ on SBA-15 was performed using a homebuilt ALD system that has been described previously [22–24]. Tetrakis (2,2,6,6-tetramethyl-3,5-heptanedionato)zirconium (Zr (TMHD) $_4$, Strem Chemicals, 99 %) and Tetrakis (2,2,6,6-tetramethyl-3,5-heptanedionato)cerium (Ce (TMHD) $_4$, Strem Chemicals, 97 %) were used as the precursors for ZrO $_2$ and CeO $_2$, respectively. For each ALD cycle, the evacuated sample was first exposed to one of the precursors at 523 K for 15 min, after which the sample as again evacuated, removed from the system, and calcined in muffle furnace at 773 K for 40 min. The growth rate was determined gravimetrically. The samples are referred to as XX-ZrO $_2$ /SBA-15 and XX-CeO $_2$ /SBA-15, where XX represents the number of ALD cycles.

 $\rm N_2$ adsorption-desorption isotherms were measured at 78 K using a Micrometrics TriStar II Plus analyzer. The samples were first heated to 573 K in a vacuum. The surface areas were then determined from the isotherms using the BET equation, and the pore size distributions were calculated using the adsorption branches with the Barret-Joyner-Halenda (BJH) method. Wide-angle XRD patterns were acquired using a Rigaku MiniFlex 6G X-ray diffractometer. TEM, Scanning Transmission Electron Microscopy (STEM), and Energy Dispersive Spectroscopy (EDS) were performed with a JEOL JEM-F200 STEM operated at 200 kV. For these measurements, the samples were diluted in ethanol

and then deposited onto carbon support films on copper grids (Electron Microscopy Sciences).

SAXS was performed at the Dual-source and Environmental X-ray Scattering (DEXS) facility at the University of Pennsylvania. The DEXS facility is equipped with a PILATUS 1 M detector for small angle scattering and a GeniX3D beam source (8 keV, Cu K α , $\lambda=1.54$ Å). Powdered samples were sealed in 1.0 mm diameter capillaries (Charles Supper Company), and 2D scattering patterns were collected at room temperature with a sample-to-detector distance of 1210 mm for 15 min. Scattering from empty capillaries was background subtracted. The isotropic scattering data was azimuthally integrated to yield I(q) plots. Data was arbitrarily vertically shifted to show data in the range 0.05 nm $^{-1} < q < 2$ nm $^{-1}$ and fit using methods described below.

3. Results

3.1. ALD of ZrO2 and CeO2 on SBA-15

The $\rm ZrO_2$ and $\rm CeO_2$ loadings on SBA-15 were monitored using the sample weight changes, with results summarized in Fig. 1 and Table S1. Fig. 1a shows changes in the mass of the sample, normalized to initial mass of SBA-15, as a function of number of ALD cycles for the two oxide films. In both cases, the mass increased almost linearly with the number of cycles, reaching values of 48-wt% after 15 Zr ALD cycles or 10 Ce ALD cycles. Fig. 1b shows the BET surface areas of these same samples as a function of the number of ALD cycles. The surface areas decreased with the number of cycles, from an initial value of $785~\rm m^2/g$, reaching values of $320~\rm m^2/g$ for $15-\rm ZrO_2/SBA-15$ and $307~\rm m^2/g$ for $10-\rm CeO_2/SBA-15$. As shown in Fig. 1c which plots the surface area normalized to the mass of SBA-15, the decreases in specific surface area are primarily due to the mass change.

The normalized growth rates can be calculated from the mass changes and surface areas in Fig. 1a and b. The initial growth rates for ZrO_2 and CeO_2 on the fresh SBA-15 were 3.8 \times 10¹⁷ Zr atoms/m²/cycle and 4.1×10^{17} Ce atoms/m²/cycle, respectively; but these increased with the number of cycles, reaching values of 9.3×10^{17} Zr atoms/m²/ cycle and 1.0×10^{18} Ce atoms/m²/cycle at the highest loadings. These values are similar in magnitude to what has been reported previously for ALD of ZrO2 and CeO2 on other supports [10,22,25,26] and are also similar in value to the coverages expected for monolayers of the very large precursor molecules used in the present study [27]. We suggest that the initial growth rates were low because reaction of the precursors with SBA-15 likely occurs at hydroxyl sites and the hydroxyl-site concentrations in the fresh SBA-15 have been shown to be low [11]. The normalized growth rate increases with coverage, to a value similar to that observed for these precursors on γ -Al₂O₃, after the initial film is formed [28].

To ensure that the $\rm ZrO_2$ and $\rm CeO_2$ films were forming inside the SBA-15 pores, the 15-ZrO₂/SBA-15 and 10-CeO₂/SBA-15 samples were examined using TEM/STEM/EDS and XRD. Fig. 2a and b show representative TEM and STEM images, with EDS maps, of the 15-ZrO₂/SBA-15 and 10-CeO₂/SBA-15 samples, respectively. The linear, well-defined pore structure of the SBA-15 support is easily observed in both cases; but there was no evidence for ZrO₂ or CeO₂ particles at the resolution of these images, even with the high oxide loadings. However, the EDS maps revealed that the pores were uniformly coated with either ZrO₂ or CeO₂, as expected.

Results from conventional XRD measurements are shown in Fig. 3 for the 15-ZrO $_2$ /SBA-15 and 10-CeO $_2$ /SBA-15 samples. No peaks characteristic of any bulk phases of ZrO $_2$ were observed on 15-ZrO $_2$ /SBA-15, consistent with an ultra-thin or amorphous ZrO $_2$ film. The diffraction patterns for 10-CeO $_2$ /SBA-15 did exhibit very broad peaks associated with the fluorite phase. Based on the peak widths and the Scherrer Equation, the average CeO $_2$ crystallite size was only 2.1 nm, a value less than the pore diameter of the SBA-15, consistent with the crystallites forming in the mesopores.

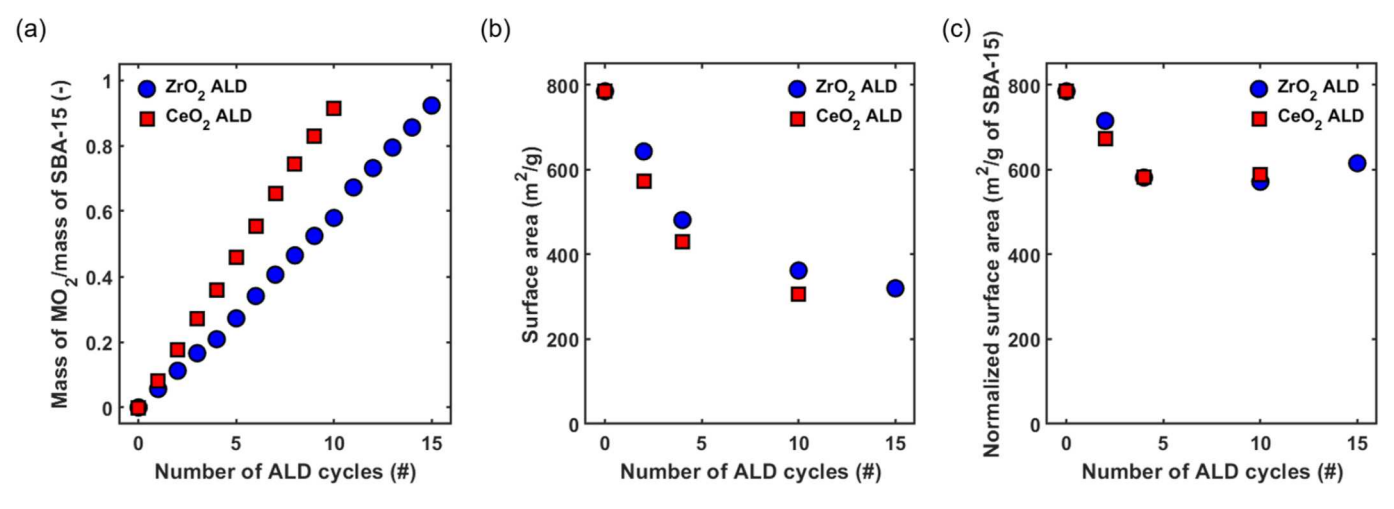


Fig. 1. (A) Plot of the mass of MO_x /mass of SBA-15 versus the number of ALD cycles (M = Zr, Ce). (b) Specific surface areas and (c) normalized surface areas of ZrO_2 / SBA-15 and CeO_2 /SBA-15 versus the number of ALD cycles.

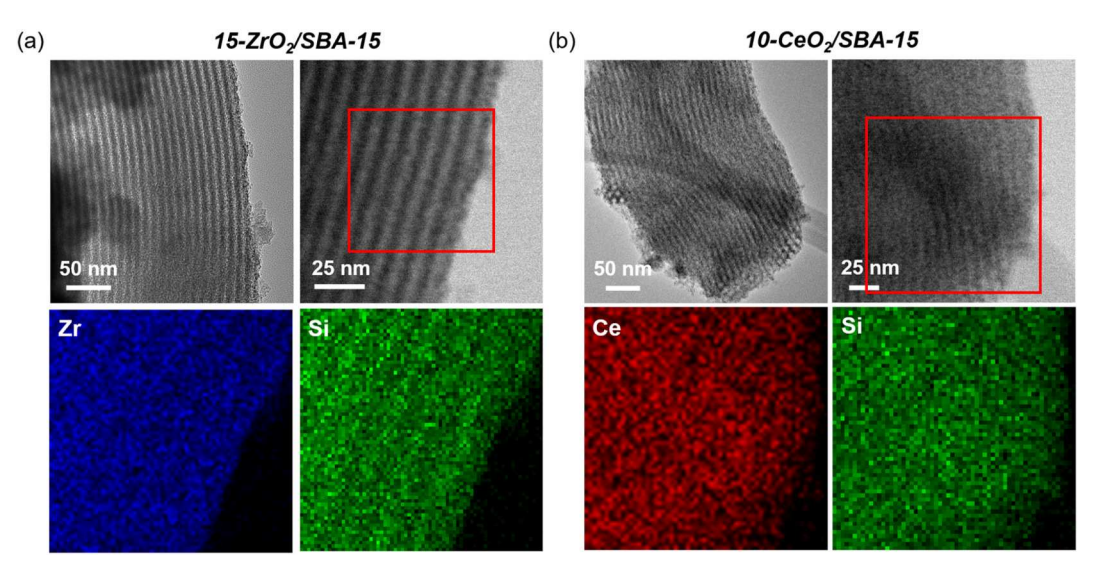


Fig. 2. Representative TEM and STEM images with EDS maps of (a) 15-ZrO₂/SBA-15 and (b) 10-CeO₂/SBA-15.

Having established that the $\rm ZrO_2$ and $\rm CeO_2$ formed inside the mesopores of the SBA-15, we next calculated the film thicknesses of the oxides using three different methods. The results of these methods are summarized in the following sections.

3.2. Film thicknesses from mass changes with bulk densities

Assuming that the films formed by each of the oxides have densities equal to that of the bulk oxides, the film thickness (t) can be calculated from the mass of the film (m), the bulk density of the oxide (ρ), and the surface area of the fresh SBA-15 (S) using Equation (1):

$$t = \frac{m}{S \times \rho} \tag{1}$$

The calculated film thicknesses are shown in Tables 1 and 2, using the densities for monoclinic ZrO_2 (5.68 g/cm³) and CeO_2 (7.22 g/cm³). While it is possible that the actual densities of the films are different from that of the bulk oxides, it is worth noting that, in the case of CeO_2 , the lattice spacing obtained from the XRD patterns is close to that of bulk CeO_2 , suggesting that the density of the CeO_2 crystallites that make up the film must be similar to that of bulk CeO_2 . At the highest loadings, the

film thicknesses for $15\text{-}ZrO_2/SBA-15$ and $10\text{-}CeO_2/SBA-15$ were calculated to be 0.21 nm and 0.17 nm, respectively.

3.3. Film thicknesses from N_2 isotherms

Film thicknesses were also determined from N_2 adsorption-desorption isotherms, in combination with the BJH Model. The isotherms, pore-size distributions, and pore volumes are shown as a function of the number of ALD cycles for ZrO_2 in Fig. 4a–c and for CeO_2 in Fig. 4d–f. In each case, the samples displayed well-defined hysteresis loops in their isotherms, indicating that the mesoporous structure was maintained throughout multiple ALD cycles. Also, each of the samples showed a well-defined peak in its pore-size distribution. The pristine SBA-15 exhibited a unimodal pore size distribution with a peak centered at 9.45 nm. For both $ZrO_2/SBA-15$ and $CeO_2/SBA-15$ samples, the pore-size distributions remained narrow and decreased systematically with the number of ALD cycles. Considering the $ZrO_2/SBA-15$ series, the pore size decreased from 9.45 nm to 6.75 nm after 15 ALD cycles. For the $CeO_2/SBA-15$ series, the pore size decreased from 9.45 nm to 6.79 nm after 10 ALD cycles.

Assuming the oxides formed uniform films over the SBA-15 pores,

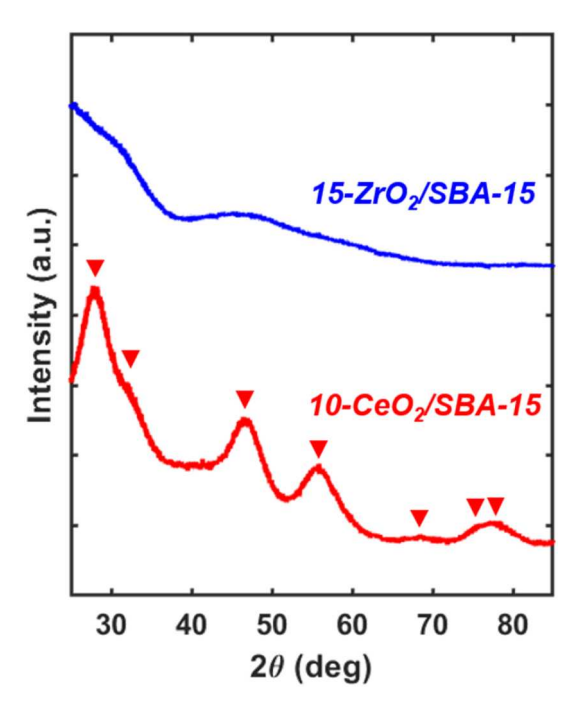


Fig. 3. XRD patterns of $15\text{-}ZrO_2/SBA\text{-}15$ and $10\text{-}CeO_2/SBA\text{-}15$. The red triangles represent the peaks corresponding to CeO_2 fluorite phase.

Table 1 Film thickness of the $\rm ZrO_2/SBA-15$ samples determined from different methods.

| Methods | Mass change with bulk density (nm) | N ₂ isotherm (nm) | SAXS (nm) |
|---------------------------------|------------------------------------|------------------------------|--------------|
| 2-ZrO ₂ /SBA- 15 | 0.03 | 0.17 | 0.06 |
| 4-ZrO ₂ /SBA- 15 | 0.06 | 0.34 | 0.18 |
| 10-ZrO ₂ /SBA- 15 | 0.15 | 0.90 | 0.33 |
| 15-ZrO ₂ /SBA- 15 | 0.21 | 1.35 | 0.50 |

Table 2 Film thickness of the $CeO_2/SBA-15$ samples determined from different methods.

| Methods | Mass change with bulk density (nm) | N ₂ isotherm (nm) | SAXS (nm) |
|---------------------------------|------------------------------------|---------------------------------|--------------|
| 2-CeO ₂ /SBA- 15 | 0.03 | 0.27 | 0.06 |
| 4-CeO ₂ /SBA- 15 | 0.07 | 0.35 | 0.16 |
| 10-CeO ₂ /SBA- 15 | 0.17 | 1.33 | 0.52 |

the film thickness should be half of the difference between the pore size of the pristine SBA-15 and ALD-coated sample. These values are reported in Tables 1 and 2 for both oxides as a function of the number of ALD cycles. It is noteworthy that the film thicknesses determined for both 15-ZrO₂/SBA-15, 1.35 nm, and 10-CeO₂/SBA-15, 1.33 nm, are similar, as should be expected since the loadings of the two oxides were both 0.92 g/g SBA-15. However, film thicknesses obtained from the isotherms are significantly greater than that determined from bulk densities by factors of 6.4 and 7.8 for ZrO₂ and CeO₂, respectively. These differences are too large to be explained in terms of densities of the films.

Fig. 4c and f show the pore volumes obtained from amounts of N_2 condensed in the pores as a function of the number of ALD cycles of ZrO_2

and CeO₂, respectively. The plots show pore volumes normalized to the total sample mass and to the mass of SBA-15. The fact that the pore volumes, normalized to the mass of SBA-15, change very little indicates pore blockage cannot be significant. These plots also provide evidence that the BJH analysis overestimates film thicknesses. The pore volume, normalized to the mass of SBA-15, should vary as the square of the pore diameter; however, the lines showing the calculated pore volumes as a function of BJH pore size in Fig. 4c and f are significantly lower than the pore volumes determined from the amount of adsorbed N₂. The plots also include lines to show how the pore volumes should decrease due to the volumes of added ZrO₂ or CeO₂, assuming bulk densities for both oxides. The measured pore volumes agree reasonably well with those calculations.

3.4. Film thicknesses from SAXS

Because SBA-15 consists of a well-defined lattice of hexagonally packed, cylindrical pores, SAXS data is expected to display peaks due to the electron density contrast between the matrix and empty pores. The intensity of these peaks is modulated by the form factor which is determined from the pore diameter. Therefore, fitting SAXS data enables the determination of the pore diameter; but, to achieve the best fits to the data, diffuse scattering must also be accounted for. The model used for fitting consists of the summation of two terms [29,30]:

$$I(q) = KS(q)P_c(q)D(q) + I_{diff}(q)$$
(2)

The first term is multiplied by a constant scaling factor, K, to allow the data to be shifted vertically so that calculated scattering intensities align well with the measured data and to account for instrumental effects, such as incident beam flux and detector efficiency. This term then includes the structure factor S(q) for a 2D hexagonal lattice, the squared form factor P_c for cylindrical pores, and the Debye-Waller factor D(q). The second term, I_{diff} , represents the diffuse scattering arising from imperfections in morphology.

For an isotropic sample, the structure factor for an undistorted lattice is given by:

$$S(q) \propto \frac{1}{q^2} \sum_{kkl} M_{hkl} G_{hkl}(q) \tag{3}$$

where $1/q^2$ is the Lorentz factor for powder diffraction, M_{hkl} is the multiplicity for Miller indices hkl, and G_{hkl} is the peak function [30]. For a 2D hexagonal lattice, scattering is not observed along the cylinder axis. Consequently, only Miller indices hk are relevant, and two-index notation is used ($M_{h0}=M_{hh}=6$, else $M_{hk}=12$). Peaks are observed at q values given by:

$$q_{hk} = \frac{4\pi}{a} \sqrt{\frac{h^2 + hk + k^2}{3}} \tag{4}$$

where a is the lattice parameter. The peak shape is represented by a pseudo-Voigt function with a Gaussian/Lorentzian mixing ratio η and full-width-at-half maximum w [29]:

$$G_{hk}(q) = \eta \frac{2}{w} \sqrt{\frac{\ln 2}{\pi}} \exp\left[-4 \ln 2\left(\frac{q - q_{hk}}{w}\right)^2\right] + (1 - \eta) \frac{2}{\pi w} \left[1 + 4\left(\frac{q - q_{hk}}{w}\right)^2\right]^{-1}$$
(5)

The form factor for cylindrical pores of radius R, with a scattering length density ρ_c in a homogenous matrix of scattering length density ρ , can be expressed as [29,30]:

$$F_c(q,R) = 2\pi(\rho - \rho_C)R^2 \frac{J_1(qR)}{qR} \approx \frac{RJ_1(qR)}{q}$$
(6)

where J_1 is the first-order Bessel function. To account for a distribution of pore sizes, a Gaussian distribution with standard deviation σ_C is

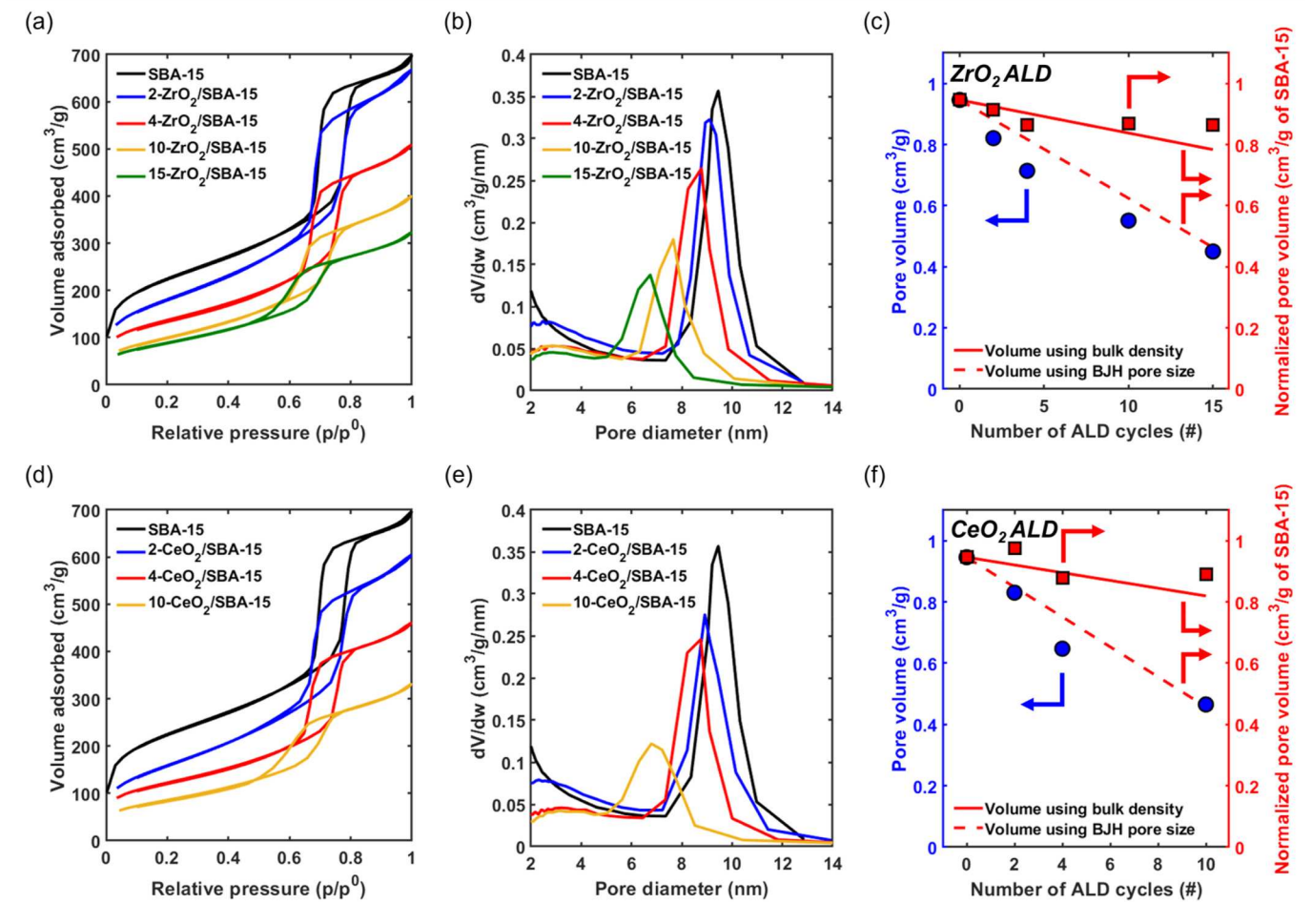


Fig. 4. (A) N_2 adsorption-desorption isotherms, (b) pore-size distributions, and (c) pore volumes as a function of ZrO_2 ALD cycles on SBA-15. (d) N_2 adsorption-desorption isotherms, (e) pore-size distributions, and (f) pore volumes as a function of ZrO_2 ALD cycles on SBA-15. In Fig. 4b and c, V and w represent pore volume and pore diameter, respectively. In Fig. 4c and f, the blue and red points indicate the pore volumes normalized to the total sample mass and to the mass of SBA-15, respectively. The solid lines show the expected pore volumes, normalize to the mass of SBA-15, assuming bulk densities for the added oxides, while the dashed lines show calculated pore volumes, normalized to the mass of SBA-15, using pore diameters from N_2 isotherms in Tables 1 and 2

assumed and used to calculate weight coefficients $w\left(R_{i}\right)$ for pores of radius R_{i} . The total contribution of the form factor is therefore:

$$P_c(q) = \sum_{i=1}^{\infty} w(R_i) |F_c(q, R_i)|^2$$
 (7)

The Debye-Waller factor is given as:

$$D(q) = \exp\left[\frac{-\sigma_{DW}^2 q^2}{2}\right] \tag{8}$$

where σ_{DW} is related to the mean-squared displacement of an atom about its average position due to thermal vibrations [29,31].

The second term in Equation (2), I_{diff} , accounts for diffuse scattering resulting from imperfections in the sample. Because SBA-15 consists of submicron sized particles, Porod scattering I_P from the interfaces of the particles will dominate at q values below q_{01} . Additionally, micropores and other inhomogeneities will give rise to diffuse scattering I_D at q values above q_{01} [30]. Finally, less well-ordered sections of the sample can give rise to broadening of the q_{01} peak that is not evident in the higher order reflections. This peak broadening is accounted for by including an additional Lorentzian peak, I_B , centered at q_{01} with a full width at half maximum w_B . In total, these contributions are modeled as [30]:

$$I_{diff} = I_P(q) + I_D(q) + I_B(q) = \frac{A_P}{q^4} + \frac{A_D}{\left(1 + \gamma^2 q^2\right)^2} + \frac{A_B w_B}{2\pi} \left[(q - q_{01})^2 + \left(\frac{w_B}{2}\right)^2 \right]^{-1}$$
(9)

where A_p is a constant related to Porod scattering, A_D and γ are constants relating to the diffuse scattering term, and A_B is a scaling factor for the Lorentzian peak.

The SAXS data and plotted fits are shown in Fig. 5, and the resulting fit parameters are included in the supporting information (See Tables S2 and S3). Acceptable fits were achieved for both the ZrO $_2$ /SBA-15 and the CeO $_2$ /SBA-15 series for all oxide coverages. Low polydispersity in pore diameters and similar pore spacings for all samples support SBA-15 having a well-defined structure that is preserved after multiple ALD cycles. For the ZrO $_2$ /SBA-15 series, fitting results show the pore diameter decreases smoothly from 8.64 nm to 7.65 nm after 15 ALD cycles indicating a final ZrO $_2$ thickness increase of 0.50 nm. Similarly, the CeO $_2$ /SBA-15 series has a pore diameter decrease from 8.64 nm to 7.60 nm after 10 ALD cycles, indicating a final CeO $_2$ film thickness of 0.52 nm. Note that the thicknesses measured by X-ray scattering are independent of the mass density of the deposited layers. Calculated film thicknesses determined from the SAXS data for the series of ZrO $_2$ /SBA-15 and CeO $_2$ /SBA-15 samples are reported in Tables 1 and 2.

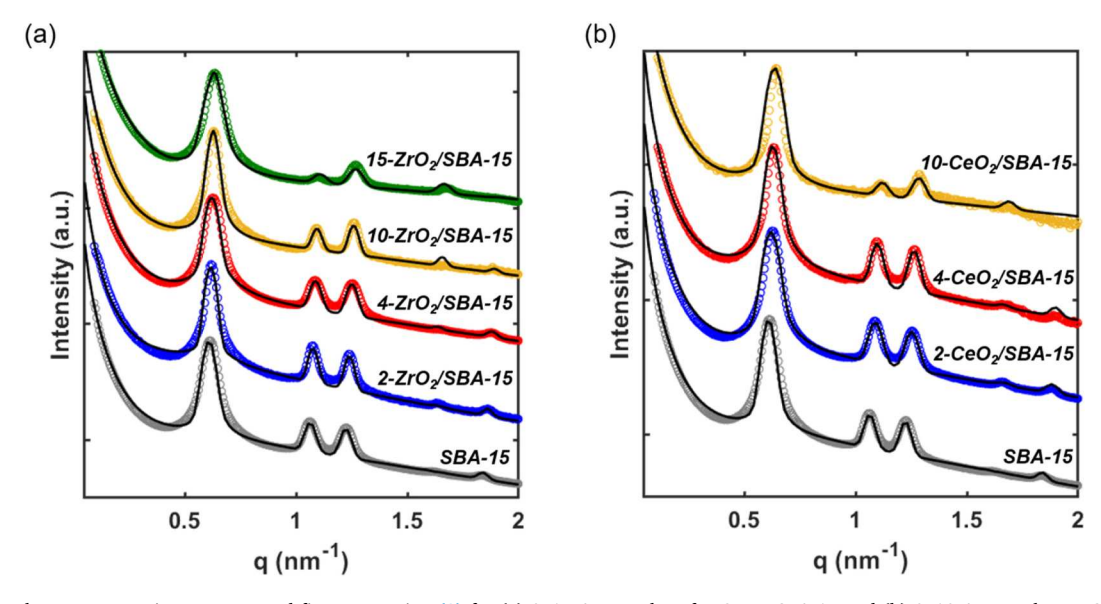
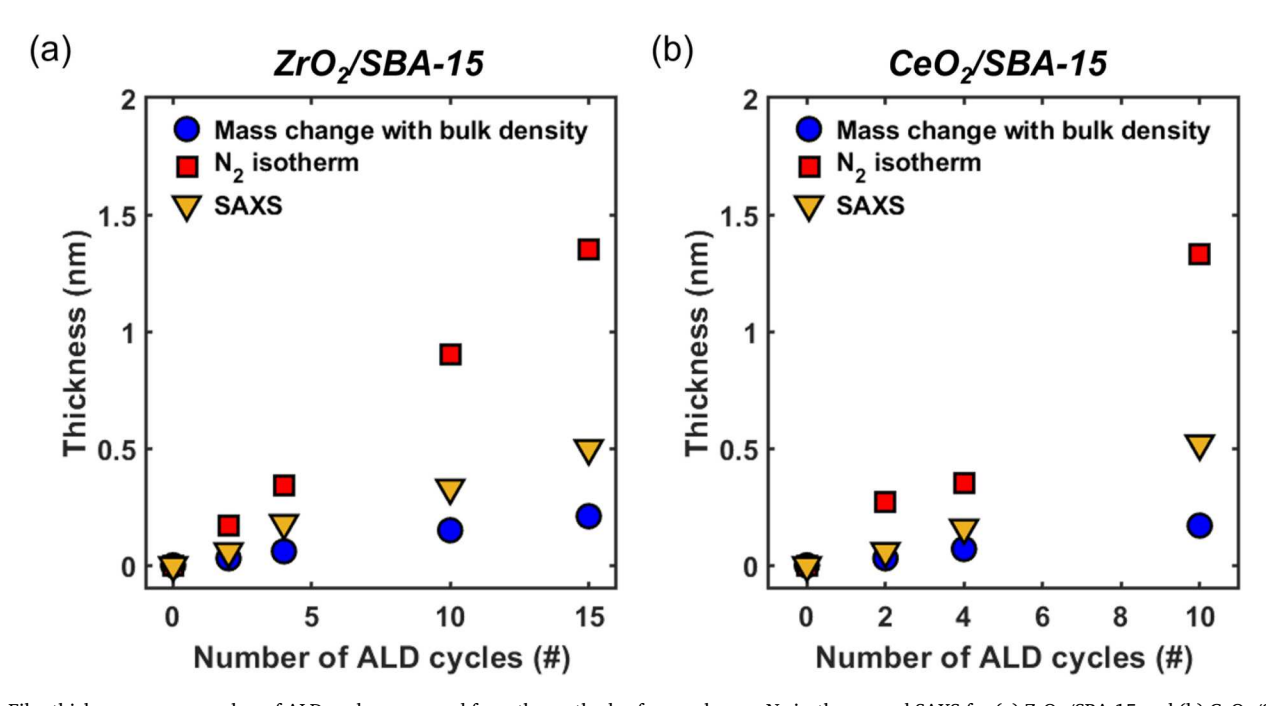


Fig. 5. Small angle X-ray scattering patterns and fits to Equation (2) for (a) 0-15 ALD cycles of ZrO₂ on SBA-15 and (b) 0-10 ALD cycles on CeO₂ on SBA-15.



 $\textbf{Fig. 6.} \ \ \textbf{Film thickness versus number of ALD cycles measured from the methods of mass change, N_2 isotherm, and SAXS for (a) ZrO_2/SBA-15 \ and (b) CeO_2/SBA-15. \\$

4. Discussion

A plot of the film thicknesses derived from mass changes, N_2 isotherms, and SAXS results is shown in Fig. 6 as a function of the number of ALD cycles for $\rm ZrO_2/SBA-15$ and $\rm CeO_2/SBA-15$. For both $\rm ZrO_2$ and $\rm CeO_2$ films, film thicknesses determined from mass changes using the bulk oxide densities provided the lowest values and film thicknesses determined from N_2 isotherms provided the highest values. Film thicknesses obtained from SAXS were between these two extremes, but closer to the values obtained from mass changes. The trends were consistent for all oxide coverages, and differences in the values obtained from the various techniques were much larger than any uncertainties in the measurements. It is important to ask why the methods give different values and to determine which value is best.

First, it is important to recognize that each of the three methods for

calculating film thickness assumes smooth, cylindrical pores. Because the size of the pores in these materials are molecular in scale, some assumptions of bulk properties will break down. The pores will not be smooth on the atomic scale, and sub-nanometer films may not have the same densities as their corresponding bulk oxides.

The question of effective film densities is worth additional attention. With the CeO_2 films, the wide-angle XRD results showed that the film was composed of CeO_2 crystallites that have a fluorite structure, with the normal lattice spacing. This implies that the bond distances and orientations are similar to that of bulk CeO_2 and that the density of the crystallites should be similar to that of the bulk material. However, it is reasonable that there could be void space between the crystallites. For example, even close packing of hard spheres would leave more than 25% voids; and less effective packing could easily increase this by a factor of two. This would be sufficient to explain the discrepancies between the

film thicknesses determined from bulk densities and SAXS. The effective film densities that one calculates from the isotherm results are much lower and not easily explained by void spaces.

Although the use of $\rm N_2$ adsorption with BJH analysis is common for determining the pore size of porous materials, studies have reported that the BJH analysis could underestimate the pore sizes of mesoporous materials with sizes less than 10 nm [17,18]. The film thicknesses are determined from changes in the measured pore sizes, and one might expect that underestimates would cancel. However, if the errors in the BJH analysis are dependent on pore size, this could explain the observed discrepancies in our study. Since the films in our case were much thinner than the pore diameter, it is surprising that the effect would be this large.

Obtaining the thickness of ALD-synthesized films through the BJH method and SAXS on conventional porous supports is obviously challenging since these supports typically have random pore sizes and structures. In our study, we leveraged the well-defined pore structure of SBA-15, combined with the ability to prepare uniform film through ALD, to determine the film thickness. This approach could provide valuable insights into ALD film growth not only on SBA-15 but also on various porous materials.

5. Conclusions

The thicknesses of ZrO_2 and CeO_2 films grown on SBA-15 by ALD were determined as a function of the number of ALD cycles using weight changes assuming bulk densities, N_2 isotherms, and SAXS. Calculations assuming bulk densities gave film thicknesses that were significantly lower than those obtained from pore-size distributions from N_2 isotherms. Film thicknesses from SAXS analysis were in reasonable agreement with thicknesses assuming bulk densities if one assumes roughly 50 % void spaces in the films.

CRediT authorship contribution statement

Ching-Yu Wang: Writing – original draft, Investigation, Formal analysis, Data curation. Benjamin T. Ferko: Writing – review & editing, Investigation, Formal analysis. Kai Shen: Investigation, Data curation. Karen I. Winey: Writing – review & editing, Supervision, Formal analysis. John M. Vohs: Writing – review & editing, Supervision, Project administration, Funding acquisition. Raymond J. Gorte: Writing – review & editing, Supervision.

Declaration of competing interest

The authors declare that they have no known competing financial interests or personal relationships that could have appeared to influence the work reported in this paper.

Data availability

Data will be made available on request.

Acknowledgements

This work was supported by the DOE BES (DE-SC0022238). Ferko acknowledges support from NSF DMR (1904767). Some of the work was performed at the Singh Center for Nanotechnology at the University of Pennsylvania, a member of the National Nanotechnology Coordinated Infrastructure (NNCI) network, which is supported by the National Science Foundation (Grant NNCI-2025608). The authors acknowledge use of the Dual Source and Environmental X-ray Scattering facility operated by the Laboratory for Research on the Structure of Matter at the University of Pennsylvania supported by NSF through (DMR-2309043).

SUPPORTING INFORMATION

Properties of the samples; fitting parameters for fits to SAXS data from $\rm ZrO_2/SBA-15$ and $\rm CeO_2/SBA-15$ samples.

Appendix A. Supplementary data

Supplementary data to this article can be found online at https://doi.org/10.1016/j.micromeso.2023.112945.

References

- P. Verma, Y. Kuwahara, K. Mori, R. Raja, H. Yamashita, Functionalized mesoporous SBA-15 silica: recent trends and catalytic applications, Nanoscale 12 (2020) 11333–11363.
- [2] S. Singh, R. Kumar, H.D. Setiabudi, S. Nanda, D.V.N. Vo, Advanced synthesis strategies of mesoporous SBA-15 supported catalysts for catalytic reforming applications: a state-of-the-art review, Appl. Catal. A-Gen. 559 (2018) 57–74.
- [3] Z. Gao, Y. Qin, Design and properties of confined nanocatalysts by atomic layer deposition, Accounts Chem. Res. 50 (2017) 2309–2316.
- [4] C.Y. Wang, J. Ra, K. Shen, J.M. Vohs, R.J. Gorte, Hydrodeoxygenation of m-cresol over WO_x-Pt/SBA-15 using alkanes as hydrogen carriers, ACS Catal. 13 (2023) 10908–10915.
- [5] D.Y. Zhao, J.L. Feng, Q.S. Huo, N. Melosh, G.H. Fredrickson, B.F. Chmelka, G. D. Stucky, Triblock copolymer syntheses of mesoporous silica with periodic 50 to 300 angstrom pores, Science 279 (1998) 548–552.
- [6] P. Hartmann, D.K. Lee, B.M. Smarsly, J. Janek, Mesoporous TiO₂: comparison of classical sol-gel and nanoparticle based photoelectrodes for the water splitting reaction, ACS Nano 4 (2010) 3147–3154.
- [7] P. Innocenzi, L. Malfatti, Mesoporous thin films: properties and applications, Chem. Soc. Rev. 42 (2013) 4198–4216.
- [8] P. Cop, S. Kitano, K. Niinuma, B.M. Smarsly, H. Kozuka, In-plane stress development in mesoporous thin films, Nanoscale 10 (2018) 7002–7015.
- [9] J.E. Herrera, J.H. Kwak, J.Z. Hu, Y. Wang, C.H.F. Peden, J. Macht, E. Iglesia, Synthesis, characterization, and catalytic function of novel highly dispersed tungsten oxide catalysts on mesoporous silica, J. Catal. 239 (2006) 200–211.
- [10] C.Y. Wang, O. Kwon, R.J. Gorte, J.M. Vohs, Synthesis of high-surface area tungstated zirconia by atomic layer deposition on mesoporous silica, Microporous Mesoporous Mater. 335 (2022), 111821.
- [11] T. Ren, C.-Y. Wang, R. Huang, C. Deng, Y. Xu, A. Majumder, J. Ra, K. Shen, J. M. Vohs, J.J. de Pablo, R.J. Gorte, D. Lee, Understanding polymer-porous solid interactions based on small gas molecule adsorption behavior, Chem. Eng. J. 473 (2023), 145220.
- [12] Z.H. Weng, Z.H. Chen, X.D. Qin, F. Zaera, Sub-monolayer control of the growth of oxide films on mesoporous materials, J. Mater. Chem. A 6 (2018) 17548–17558.
- [13] Y.J. Pagan-Torres, J.M.R. Gallo, D. Wang, H.N. Pham, J.A. Libera, C.L. Marshall, J. W. Elam, A.K. Datye, J.A. Dumesic, Synthesis of highly ordered hydrothermally stable mesoporous niobia catalysts by atomic layer deposition, ACS Catal. 1 (2011) 1234–1245.
- [14] W. Ke, X.D. Qin, R.M. Palomino, J.P. Simonovis, S.D. Senanayake, J.A. Rodriguez, F. Zaera, Redox properties of TiO₂ thin films grown on mesoporous silica by atomic layer deposition, J. Phys. Chem. Lett. 14 (2023) 4696–4703.
- [15] W. Ke, Y. Liu, X.L. Wang, X.D. Qin, L.M. Chen, R.M. Palomino, J.P. Simonovis, I. Lee, I. Waluyo, J.A. Rodriguez, A.I. Frenkel, P. Liu, F. Zaera, Nucleation and initial stages of growth during the atomic layer deposition of titanium oxide on mesoporous silica, Nano Lett. 20 (2020) 6884–6890.
- [16] S. Sato, M. Toita, T. Sodesawa, F. Nozaki, Catalytic and acidic properties of silicaalumina prepared by chemical vapor-deposition, Appl. Catal. 62 (1990) 73–84.
- [17] J. Villarroel-Rocha, D. Barrera, K. Sapag, Introducing a self-consistent test and the corresponding modification in the Barrett, Joyner and Halenda method for poresize determination, Microporous Mesoporous Mater. 200 (2014) 68–78.
- [18] B. Coasne, K.E. Gubbins, R.J.M. Pellenq, A grand canonical Monte Carlo study of adsorption and capillary phenomena in nanopores of various morphologies and topologies: testing the BET and BJH characterization methods, Part. Part. Syst. Char. 21 (2004) 149–160.
- [19] C.Y. Wang, K. Shen, R.J. Gorte, J.M. Vohs, Preparation of SBA-15-supported metals by vapor-phase infiltration, Inorganics 10 (2022) 215.
- [20] S. Lee, K. Shen, C.Y. Wang, J.M. Vohs, R.J. Gorte, Hydrogenolysis of n-eicosane over Ru-based catalysts in a continuous flow reactor, Chem. Eng. J. 456 (2023), 141030.
- [21] C.-Y. Wang, J.M. Vohs, R.J. Gorte, Dehydrogenation of cycloalkanes over Pt/SBA-15 for endothermic cooling, Fuel 357 (2024), 129780.
- [22] T.M. Onn, S.Y. Zhang, L. Arroyo-Ramirez, Y. Xia, C. Wang, X.Q. Pan, G.W. Graham, R.J. Gorte, High-surface-area ceria prepared by ALD on Al₂O₃ support, Appl. Catal. B Environ. 201 (2017) 430–437.
- [23] T.M. Onn, R. Kungas, P. Fornasiero, K. Huang, R.J. Gorte, Atomic layer deposition on porous materials: problems with conventional approaches to catalyst and fuel cell electrode preparation, Inorganics 6 (2018) 34.
- [24] T.Y. Cao, C.Y. Wang, K. Shen, J.M. Vohs, R.J. Gorte, Investigation into support effects for Pt and Pd on LaMnO₃, Appl. Catal. A-Gen. (2022) 646.

- [25] T.M. Onn, S.Y. Zhang, L. Arroyo-Ramirez, Y.C. Chung, G.W. Graham, X.Q. Pan, R. J. Gorte, Improved thermal stability and methane-oxidation activity of Pd/Al₂O₃ catalysts by atomic layer denosition of ZrO₂. ACS Catal. 5 (2015) 5696–5701.
- catalysts by atomic layer deposition of ZrO₂, ACS Catal. 5 (2015) 5696–5701.

 [26] K. Shen, J. Chang, R.K. Rai, C.Y. Wang, E.A. Stach, R.J. Gorte, J.M. Vohs, Thermodynamic and structural properties of bulk and thin-film CeVO₄ and LaVO₄, J. Phys. Chem. C 127 (2023) 15591–15599.
- [27] R.L. Puurunen, Growth per cycle in atomic layer deposition: real application examples of a theoretical model, Chem. Vap. Depos. 9 (2003) 327–332.
- [28] X.Y. Mao, A. Foucher, E.A. Stach, R.J. Gorte, A study of support effects for CH₄ and CO oxidation over Pd catalysts on ALD-modified Al₂O₃, Catal. Lett. 149 (2019) 905–915.
- [29] Y. Ishii, Y. Nishiwaki, A. Al-zubaidi, S. Kawasaki, Pore size determination in ordered mesoporous materials using powder X-ray diffraction, J. Phys. Chem. C 117 (2013) 18120–18130.
- [30] A. Zelenakova, P. Hrubovcak, O. Kapusta, N. Kucerka, A. Kuklin, O. Ivankov, V. Zelenak, Size and distribution of the iron oxide nanoparticles in SBA-15 nanoporous silica via SANS study. Sci. Rep. 9 (2019).
- nanoporous silica via SANS study, Sci. Rep. 9 (2019).

 [31] R.J. Roe, Methods of X-Ray and Neutron Scattering in Polymer Science, Oxford University Press, New York, 2000.